Article

Evaluation of P-Band SAR Tomography for Mapping Tropical Forest Vertical Backscatter and Tree Height

Naveen Ramachandran [1],*, Sassan Saatchi [2], Stefano Tebaldini [3], Mauro Mariotti d'Alessandro [3] and Onkar Dikshit [1]

1 Department of Civil Engineering, Indian Institute of Technology Kanpur, Kanpur 208016, India; onkar@iitk.ac.in
2 Jet Propulsion Laboratory (JPL), California Institute of Technology, Pasadena, CA 91125, USA; sasan.s.saatchi@jpl.nasa.gov
3 Dipartimento di Elettronica, Informazione e Bioingegneria, Politecnico di Milano, 20133 Milan, Italy; stefano.tebaldini@polimi.it (S.T.); mauro.mariotti@polimi.it (M.M.d.)
* Correspondence: naveenr@iitk.ac.in

Abstract: Low-frequency tomographic synthetic aperture radar (TomoSAR) techniques provide an opportunity for quantifying the dynamics of dense tropical forest vertical structures. Here, we compare the performance of different TomoSAR processing, Back-projection (BP), Capon beamforming (CB), and MUltiple SIgnal Classification (MUSIC), and compensation techniques for estimating forest height (FH) and forest vertical profile from the backscattered echoes. The study also examines how polarimetric measurements in linear, compact, hybrid, and dual circular modes influence parameter estimation. The tomographic analysis was carried out using P-band data acquired over the Paracou study site in French Guiana, and the quantitative evaluation was performed using LiDAR-based canopy height measurements taken during the 2009 TropiSAR campaign. Our results show that the relative root mean squared error (RMSE) of height was less than 10%, with negligible systematic errors across the range, with Capon and MUSIC performing better for height estimates. Radiometric compensation, such as slope correction, does not improve tree height estimation. Further, we compare and analyze the impact of the compensation approach on forest vertical profiles and tomographic metrics and the integrated backscattered power. It is observed that radiometric compensation increases the backscatter values of the vertical profile with a slight shift in local maxima of the canopy layer for both the Capon and the MUSIC estimators. Our results suggest that applying the proper processing and compensation techniques on P-band TomoSAR observations from space will allow the monitoring of forest vertical structure and biomass dynamics.

Keywords: forest structure; LiDAR; Polarimetry; SAR Tomography; TropiSAR

1. Introduction

Tropical forests are crucial for understanding the global carbon cycle and its impact on climate dynamics [1,2]. Monitoring forest vertical structure and tree height plays a vital role in the functioning and management of the ecosystem [3–5]. Knowledge about the structural dynamics allows us to assess the impacts of natural and human-induced processes on the evolution of forest ecosystems. Such information at fine spatial resolutions serves as an indicator for detecting changes due to deforestation, degradation, and regeneration phenomena [6,7], and helps in understanding how these changes influence the forest function and the climate system [8,9]. Further, vertical forest structure is essential information for the development of an accurate biomass map. Biomass estimates over tropical forests are still a large source of uncertainty compared to their counterparts [10,11] and have to be improved to better represent tropical forests for the projection of climatic scenarios in global models. The spatial and temporal dynamic nature of the forest ecosystem makes it challenging to monitor and characterize its structure via traditional field

sampling at regional or global scales. The complex, diverse, and dynamic nature of tropical forests demands a new approach to surveying and examining the three-dimensional (3D) distribution of the ecosystem. Remote sensing imaging techniques from active sensors such as multi-baseline synthetic aperture radar (SAR) systems have been shown to be a promising approach for monitoring forest 3D structures [12–18].

The traditional interferometric approach exploits the phase difference between two images to retrieve the tree height [19–21]. However, it fails to differentiate targets along the vertical direction. The tomographic approach overcomes this limitation and allows separation of the target along the vertical direction by synthesizing an aperture in a vertical direction using multi-baseline data acquired at a slightly different geometry [15]. The first experimental validation of tomographic synthetic aperture radar (TomoSAR) was demonstrated in [22] and realized for earth observation using airborne L-band data [15]. Subsequently, techniques for retrieving the vertical structure of forests from TomoSAR observations were developed using non-parametric [15,23–27], parametric [23–25,27–29], and hybrid [23,30–33] approaches. Non-parametric approaches do not rely on a priori information about the forest structure, while parametric approaches are based on assumptions about the model used for the parametrization of forest media. While the former suffers from the number and sampling of baselines [16], the later depends on the selection of models. The hybrid approach provides a constrained solution without making any assumptions [18,30,32,33].

The purpose of this article is two-fold. Firstly, we investigate and compare the performance of the most commonly used tomographic inversion approaches (Back-projection, Capon and MUSIC) to retrieve tropical forest vertical structure and tree height at different polarizations. Here, the vertical forest structure is indicated by the 3D distribution of backscattered power along the vertical direction. Even though these tomographic estimators have been widely used to estimate the vertical structure of forests, here we put the emphasis on the comparison of their performance to estimate the forest tree height. Further, the estimation of forest vertical structure has been mostly limited to linear polarization data and has ignored circular polarizations, particularly if they are important for improving low-frequency (P-band) SAR radiometry in the presence of ionospheric interferences [34,35]. Secondly, the backscattered signal from the SAR data is influenced by both surface characteristics, such as soil and canopy moisture, and topographic relief. The perturbation of backscatter signal as a result of variation in surface and double-bounce scattering due to local terrain relief was demonstrated in [36,37]. Such distortions have to be accounted for before parameter retrieval. The slope compensation approach, such as that adopted in Minh et al. [17], has been shown to minimize the effect of ground contribution. However, as we move from near- to far-range, the irregular resolution cells in the cross-range direction result in variable volume size, and its effect on backscattered power has not been addressed yet. Hence, we plan to introduce a volumetric compensation approach to compensate for the terrain relief on TomoSAR data. For super-resolution techniques such as Capon and MUSIC, which do not preserve the radiometric property and provide pseudo-spectrum, it is essential to provide a compensation approach to address the radiometric property and provide reasonable correlation with different layers of the tomographic stack. Here, we compare the effects of these compensation approaches on the backscatter power of different layers and their influence on height and forest vertical structure estimation. The analysis is performed using P-band airborne data from the ESA TropiSAR 2009 campaign over Paracou, French Guiana.

This paper is organized as follows: In Section 2, we summarize the conceptual framework of Tomographic SAR and the different inversion techniques adopted. Section 3 discusses three different compensation approaches adopted to compensate for the perturbation in the backscatter power. The results and analysis of experiments performed on the P-band dataset are presented and discussed in Section 4. Finally, in Section 5, conclusions are drawn.

2. SAR Tomography

2.1. Signal Model and Inversion Approaches

The fundamental objective of TomoSAR is to reconstruct the vertical reflectivity profiles for each range-azimuth pixel by focusing in the vertical direction. This is achieved by using multiple SAR images acquired at different sensor positions. Let us consider a simplified geometry of multi-baseline SAR acquisition with N-baseline (Figure 1). For simplicity, we assume an ideal condition such that the wave penetration over the entire volume and baselines is equally spaced. After SAR images are focused and co-registered with respect to the master image, the resulting return in the nth SAR image from the scatterers can be modeled as follows [38].

$$S_n(x', r') = \iint f(x' - x, r' - r) dx dr \int \gamma(x, r, v) . e^{\left(-j \frac{4\pi}{\lambda} R_n(r,v)\right)} dv; n = 1, 2 \cdots, N, \quad (1)$$
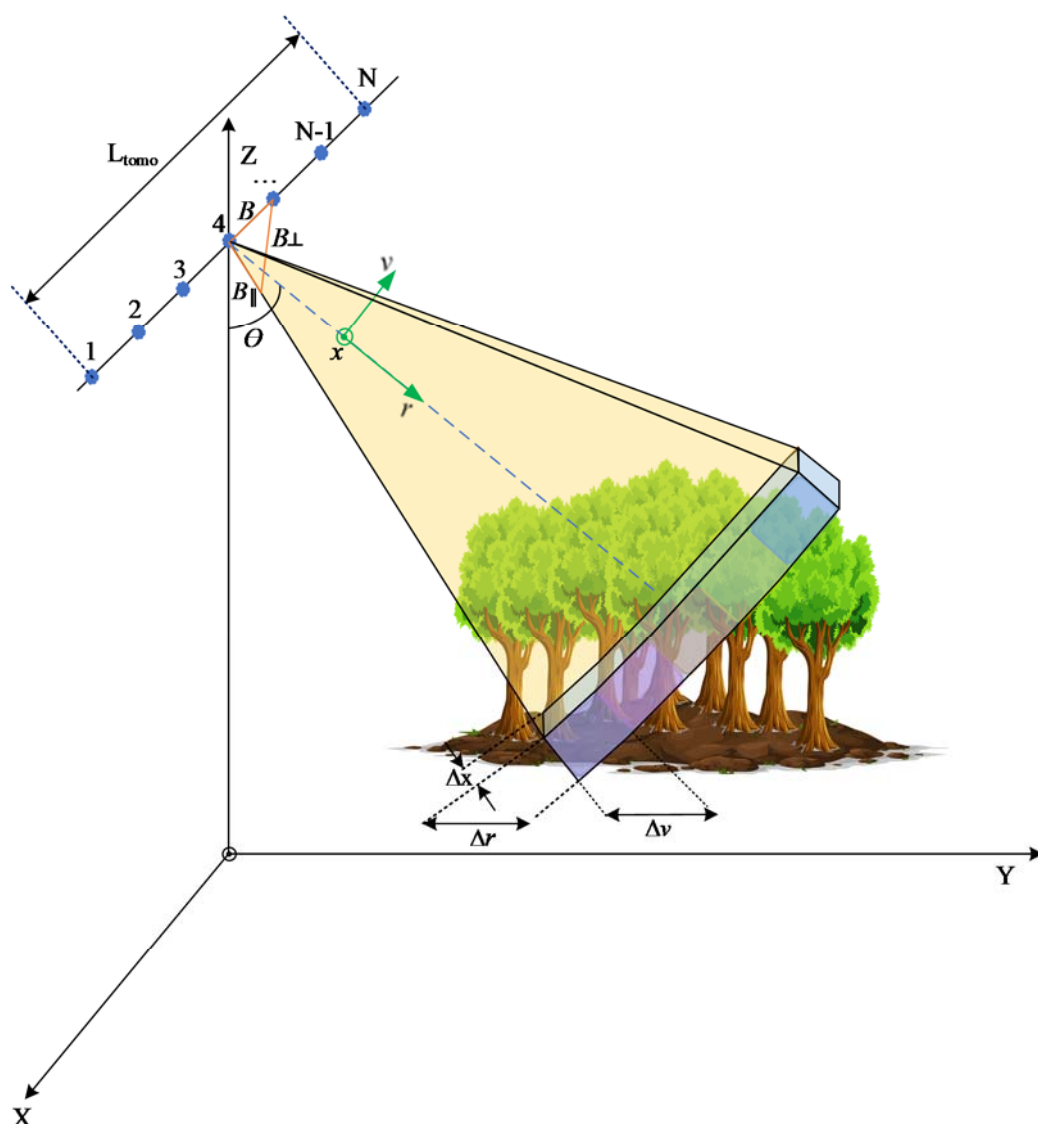

Figure 1. Simplified geometry of multiple baseline synthetic aperture radar (SAR) tomography. L_{tomo}—Tomographic aperture length, (X, Y, Z)—global coordinate system, (x, r, v)—SAR coordinates system, $(\Delta x, \Delta r, \Delta v)$—azimuth, slant- and cross-range resolution, θ—radar look angle, $(B, B_\parallel, B_\perp)$—baseline, parallel baseline, and perpendicular baseline, respectively.

Here, $\gamma(\cdot)$ is the scene complex reflectivity; x, r, and v are the azimuth, slant-, and cross-range positions, respectively; $R_n(r, z, v)$ denotes the distance between the sensor position and the target (r_0, v_0) for the nth pass; and f is the space invariant post focusing

two-dimensional (2D) point spread function (PSF). The calibration of the phase term from topography and uncompensated phase disturbance (atmospheric delay and baseline estimation error), which corrupts the phase of the image [39], will result in the calibrated tomographic data stack that can be expressed as [38,39]:

$$S_n(x,r) = \int \gamma(x,r,\ v)e^{jK_z v}dv \qquad (2)$$

Here, $S_n(x,r)$ denotes the complex-valued pixel located at azimuth-slant-range position (x,r) from nth sensor, $\gamma(x,r,v)$ is the average complex reflectivity within the azimuth-slant-range resolution cell, v is the cross-range coordinate perpendicular to platform motion and direction of the radar signal, and K_z represents the vertical wavenumber and is related to the Height of Ambiguity (*HoA*) between the interferometric pair as:

$$K_z = \frac{2\pi}{HoA} = \frac{4\pi}{\lambda r_0}b_n \qquad (3)$$

Here, b_n is the perpendicular baseline with respect to the master image, λ is the signal wavelength, and r_0 is the distance from the sensor to the scatterer. For any fixed azimuth-range index, the calibrated signal from different sensor positions can be represented as samples of Fourier transform of the reflectivity function along the vertical direction [15]. The spectral analysis of Equation (1), using fast Fourier transform, results in a pixel of focused SAR image from the nth pass that can be related to the vertical distribution of the scatterer in the cross-range direction via Fourier transform.

$$P_{BP}(z) = \gamma(x,r,\ v) = \sum_{n=1}^{N} S_N(x,r)e^{(-jK_z v)}dv \qquad (4)$$

The approach expressed in Equation (4) is known as the back-projection (BP) approach or tomographic focusing [15,17,40,41], which allows us to retrieve the distribution of backscattered power in the cross-range direction. The key parameters that characterize the efficiency of the inversion approach is geometrical resolution in the cross-range and can be expressed as [15]:

$$\Delta v \approx \frac{\lambda r_0}{2.L_{tomo}} \approx \frac{2\pi}{Max(K_z) - Min(K_z)}\sin\theta \qquad (5)$$

Here, L_{tomo} is the total length of synthetic aperture achieved in the vertical direction. However, the realistic multi-baseline scenario suffers from irregular baseline and temporal decorrelation. This results in height ambiguities due to non-uniform sampling and degradation of vertical resolution, resulting in anomalous sidelobes, which affects the radiometric quality. The application of super-resolution techniques such as Capon and MUSIC improves the imaging capability and provides better resolution than the BP approach. Capon [23–25,42–44] is the most widely used non-parametric approach and is viewed as a solution for the minimization problem, as defined in [23,44–47], which constitutes the average power of the capon estimator.

$$P_{Capon}(z) = \frac{1}{a^H(z)\cdot\hat{R}^{-1}\cdot a(z)} \qquad (6)$$

Here, P_{Capon} is the backscattered power estimated using the Capon estimator. The MUSIC estimator is a subspace-based technique that exercises the Eigen-decomposition of covariance, $\hat{R}$, into orthogonal signal and noise subspaces. This estimation approach is considered to be a model-based approach from the fact that they assume the signals to be a superposition of multiple point-like sources.

$$P_{MUSIC}(z) = \frac{1}{a^H(z)\cdot W_n^H W_n\cdot a(z)} \qquad (7)$$

Here, P_{MUSIC} is the backscattered power estimated using the MUSIC estimator, $\hat{R}$ is estimated covariance matrix, $a(z)$ denotes the steering vector given by Equations (8) and (9), and W_n denotes the Eigenvectors of the noise subspace. The noise subspace is estimated by the Eigen decomposition of the $\hat{R}$ matrix.

$$\hat{R} = \frac{1}{N}\sum_{n=1}^{N} S_n(x,r)S_n{}^{*}(x,r) \tag{8}$$

$$a(z) = \begin{bmatrix} 1, & exp(jK_{z_2}z), & \exp(jK_{z_3}z), & \ldots, & exp(jK_{z_K}z) \end{bmatrix}^T \tag{9}$$

The resolution in the vertical direction can be expressed by the exploitation of a simple geometrical relation, $z = v.\sin\theta$, where θ is the elevation angle.

2.2. Tomographic Compensation

To achieve a robust solution and the accuracy of parameters within the desired values, it is essential to account for factors that distort the tomographic signal. Before starting the parameter retrieval, it is important to review the impact of different compensation approaches used to minimize the effect of these distorting factors on the estimation of biophysical parameters.

2.2.1. Radiometric Compensation

Although the Capon and MUSIC estimators provides better vertical resolution, the radiometric quality is not preserved. The estimators provide a pseudo spectrum rather than a true spectrum. Hence, when we relate a physical quantity such as the forest structure or biomass to the backscatter power from the tomograms, it results in lesser variations in correlation with different layers of the tomograms. To achieve a meaningful relationship between backscatter values, scattering mechanism, and the physical quantity, we compensate the backscatter at each layer by multiplying it by the backscattered power of the master image. In this study, we have used the backscatter of the master image (I_M) in the linear unit. The compensation can be expressed as follows:

$$\left.\begin{array}{l} P_E^R(x,g,\ z) = |\gamma(x,g,\ z)|^2 * I_M; \\ \text{Here,}\ I_M = |S_M(x,g,z)|^2 \end{array}\right\} \tag{10}$$

where, $\gamma(x,g,\ z)$ denotes the complex-valued reflectivity corresponding to an azimuth-ground range cell at an elevation, z, of a tomographic stack, $P_E^R(x,g,z)$ is the radiometrically compensated backscattered power, E stands for Capon or MUSIC estimators, and $S_M(x,g,z)$ is the master image.

2.2.2. Slope Compensation

The SAR signal from the vegetation is expressed as a sum of the contribution from vegetation and underlying terrain characteristics [48,49]. The works by [36,37] discuss the correlation of terrain slope with backscatter at different layers of tomograms. The effect of topographic slope variation on tomographic backscatter layers is discussed and validated from the above-ground biomass (AGB) estimation point of view in [40]. These results indicate the importance of removing the terrain slope from the tomographic layers when estimating forest structure and biomass. The tomographic slope compensation can be expressed, as in [40], in the ground range geometry:

$$P_{BP}^s(x,g,\ z) = |\ \gamma(x,g,\ z)|^2 \cdot \sin(\theta - \alpha) \tag{11}$$

Here, $P_{BP}^s(x,g,\ v)$ is the slope compensated backscattered power. Further θ and α denote the radar elevation angle and the local slope in the ground range geometry, respectively.

2.2.3. Volumetric Compensation

As a result of geometric distortion due to incidence angle and slope, the cell resolutions in a slant- and cross-range vary from near- to far-range, resulting in inconsistent volume area covered on the ground. Hence, it is essential to compensate for the volumetric area before relating the backscatter power to any geophysical parameter at the ground level. Here, we begin by assuming that the volume layer is a collection of randomly oriented identical scatterers exhibiting independent scattering effects on the total backscatter. Then, the backscattering coefficient of the 3D resolution cell can be expressed as the summation of backscattering from each scatterer within that resolution cell. Hence, to compensate for the backscattering, volumetric content can be given as follows:

$$\left. \begin{array}{c} P_{BP}^{v}(x, g, z) = \frac{|\gamma(x, g, z)|^2}{V_c}; \\ \text{Here, } V_c = \Delta x \cdot \Delta g \cdot \Delta z = \Delta x * \Delta g * \frac{\Delta v}{\sin(\theta - \alpha)} \end{array} \right\} \tag{12}$$

Here, Δx, Δg, Δz, Δr and Δv are the azimuth, ground, vertical, slant- and cross-range resolutions, respectively. The cross-range resolution for the BP approach is expressed as in Equation (4), and for other conventional covariance-based estimators, discussed above, is given by the interval at which the tomograms are estimated in the vertical direction. For example, we have estimated tomograms at an interval of 1 m for the Capon and MUSIC estimators. Hence, in our case, both slope and volumetric compensations converge to similar results scaled by a constant variable, V_c, at volume intervals $\Delta v = 1$.

3. Materials and Methods

3.1. Materials

Our study site was over the Paracou field station (5°18′N, 52°55′W), located in a lowland moist tropical forest with high above-ground biomass (up to 450 t/ha) near Sinnamary, French Guiana. The elevation at the site is between 5 and 50 m, and the mean annual temperature is 26 °C, with an annual range of 1.0–1.5 °C. Rainfall averages 2980 mm yr^{-1} (30-year period), with a three-month dry season (<100 mm month^{-1}) from mid-August to mid-November. The landscape is characterized by a patchwork of hills (100–300-m wide and 20–35-m high), separated by narrow streams. The forest in Paracou is classified as a lowland moist forest with 140–200 species per hectare, as specified in the forest census of all trees with a diameter at breast height (DBH) >10 cm [50,51]. The analysis of the vertical structure and tree height estimation were performed over the 16 permanent experimental plots, which were sub-divided into plots of 1-ha, 2-ha, 3-ha, and 4-ha resolutions. The average canopy height is marked at around 30 m, with a maximum reach of up to 45 m and biomass varying between 200–450 t/ha across these plots. We also had access to 2009 data from an airborne LiDAR scanning (ALS) system using a RIEGL LMS-280i onboard a helicopter, which was collected over an area of 1100 ha at high spatial resolution (1-m) with approximately 5.7 points/m^2 [52]. LiDAR-derived Canopy Height Model (CHM) was used to validate the forest height and vertical forest structure.

We used data from the P-band airborne TropiSAR campaign from the summer of 2009 from the framework of the European Space Agency BIOMASS mission calibration and validation activities. The main campaign objectives were to evaluate how P-band radar imaging of tropical forests in different polarimetric, interferometric, and tomographic modes would perform in the estimation of forest height and AGB. The tomographic data were acquired with six fully polarimetric images at P-band, each separated by 15.24 m vertically above the master at equal intervals using a SETHI airborne SAR system from ONERA. The mean values of the vertical wavenumber between the interferometric pair over the region of interest, shown in Figure 2, were 0.0518, 0.1193, 0.1624, 0.1978 and 0.2747 rad/m, respectively. The sensor operated with a frequency centralized at 397.5 MHz with a bandwidth of 125 MHz. The waveform is characterized by a typical swath of 5 km with an incidence angle ranging from 25° to 60° flying at an altitude of 4014 m.

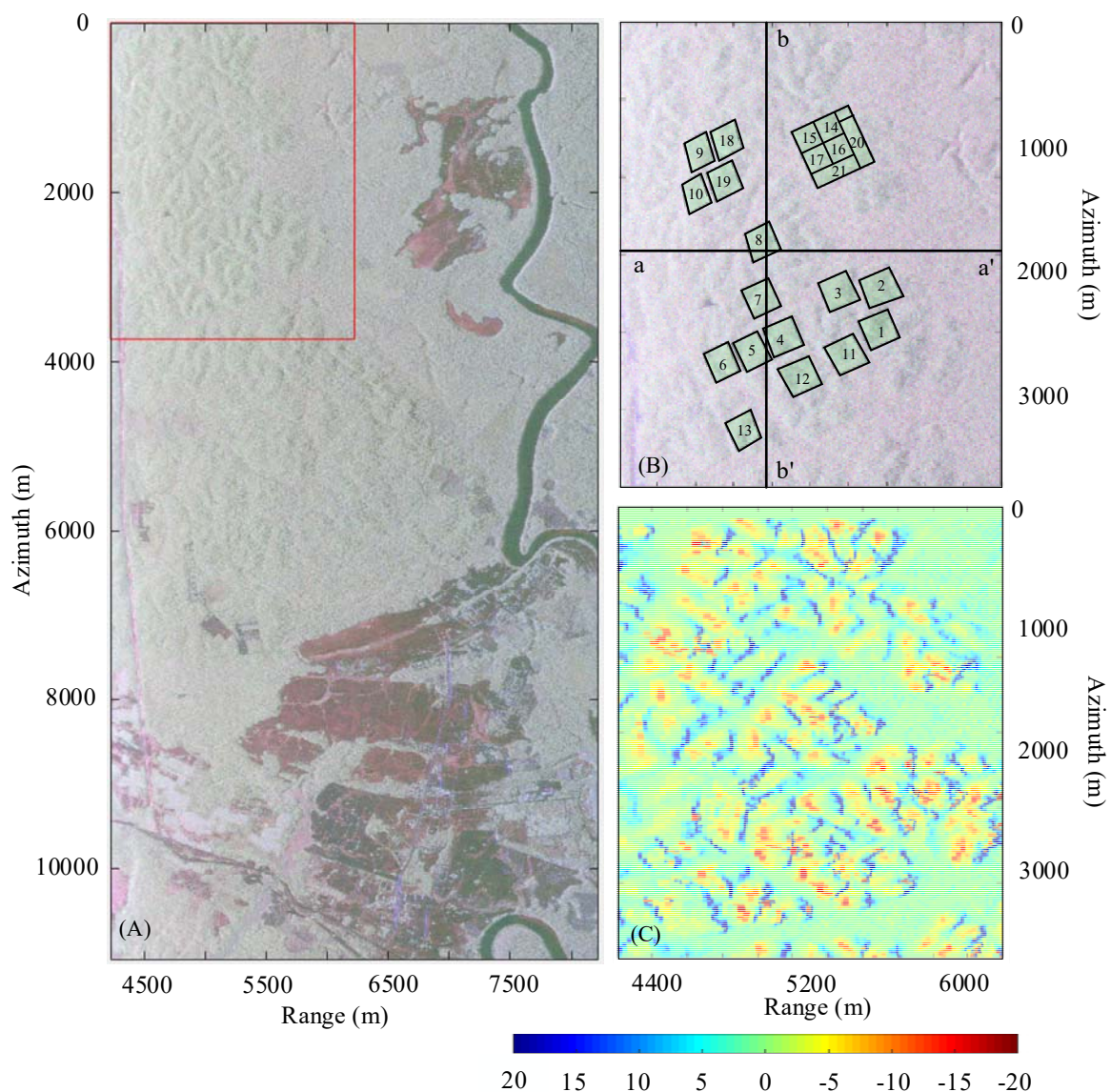The SLC image had a pixel spacing of 1 m and 1.245 m in slant range and azimuth direction, respectively.

Figure 2. Paracou test site: (**A**) P-band SAR image (4000 × 8895 pixels) covering an area 6 km wide by 10 km long. The red box indicates the region of interest (ROI) of this study; (**B**) Pauli RGB (Red: |HH-VV|; Green: |2HV|; Blue: |HH+VV|) image over the ROI. Here, the lines aa′ corresponds to fixed azimuth value (1838.9 m) over which the tomographic profiles are displayed; (**C**) displays the slope over the ROI. The range has been scaled between −20 and 20 degrees for better visualization.

3.2. Methods

The extraction of forest biophysical parameters via the tomographic approach can be divided into three main blocks, as shown in Figure 3: interferometric processing; tomographic processing and parameter retrieval and validation. The interferometric processing begins with the selection of a master image from the stack of SAR images acquired at slightly different geometry (orbits from satellite, flight tracks from airborne platforms). The selection of the master image plays a vital role as it influences the outcome. The slave images are then co-registered at the sub-pixel level and resampled to the master image geometry. Later, flat-earth corrections are applied to the interferometric stack. Because radar techniques measure the phase delay, any occurring propagation disturbance can corrupt the phase signals and has to be accounted for before further processing. The

procedure for estimating and removing phase offsets due to propagation disturbances is known as phase calibration [39,53,54]. In this work, the tomographic stack over the Paracou study site was calibrated using the Phase Center Double Localization approach (PCDL) [55]. This approach can be considered as a two-step procedure: (1) estimating the phase-linked errors and (2) solving them to estimate the sensor and target positions.
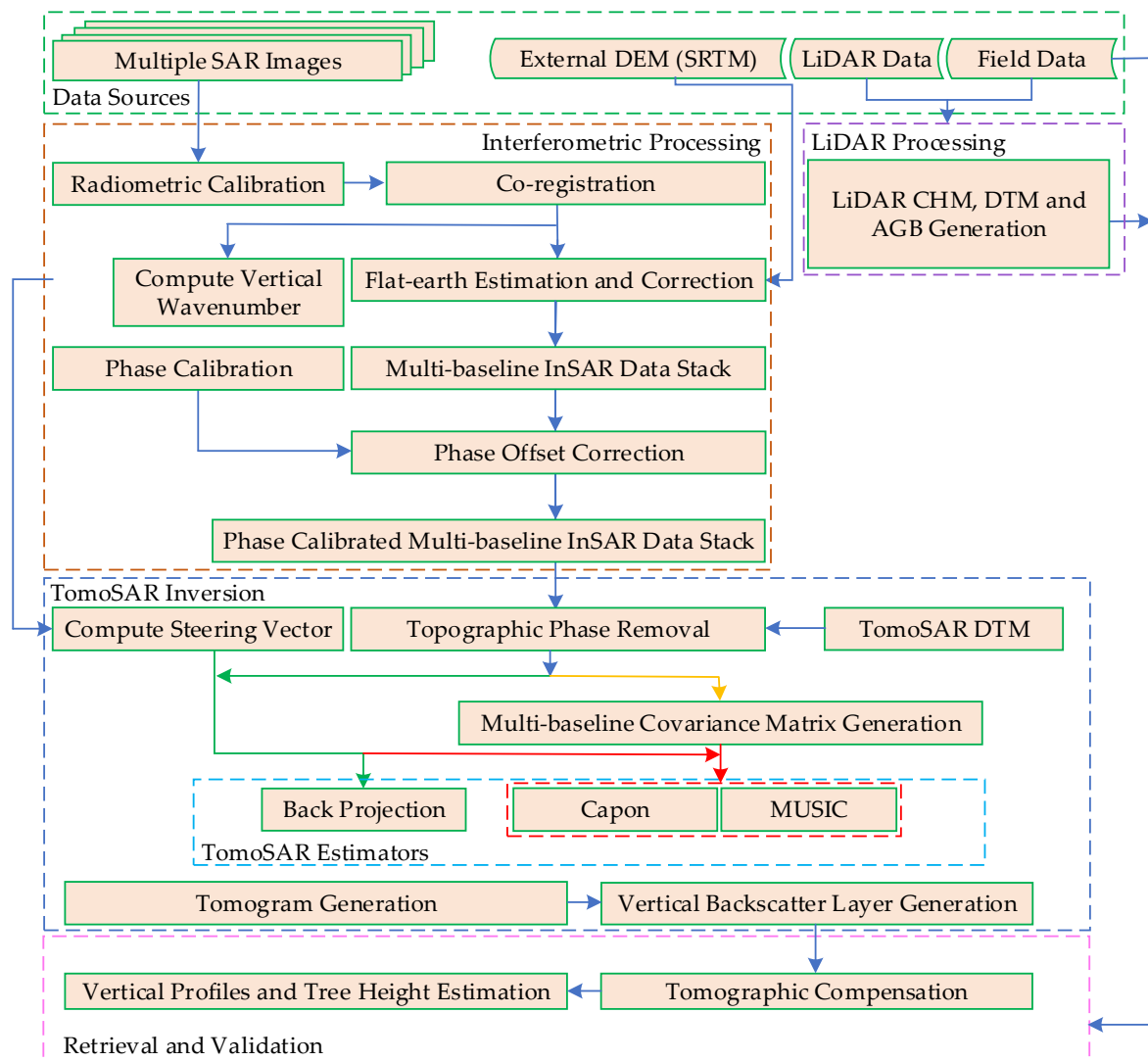
Figure 3. The flowchart of biophysical parameter estimation using SAR Tomography. Here, DEM and DTM represents digital elevation and terrain models respectively, SRTM represents Shuttle Radar Topography Mission and InSAR and TomoSAR represents interferometric and tomographic synthetic aperture radar.

The phase calibration procedure allows us to perform focusing along the elevation direction. The tomographic processing begins with the removal of phase offsets due to terrain topography. The knowledge of accurate terrain topography has a significant impact on the TomoSAR focusing as it is essential for (a) removing terrain topography and focus contribution with respect to zero references and (b) accounting for the contribution of terrain slope on backscattered power. The terrain topography was estimated via the approach discussed in Mariotti d'Alessandro and Tebaldini [56], which the reader can refer to for further details. Once the data stack is corrected for propagation disturbance and topographic offsets, the multi-baseline interferometric coherence is estimated. The tomographic inversion is carried out, as discussed in the above section, to generate a tomographic cube.

To relate the tomogram to the in-situ data, it is necessary to convert the tomogram from radar geometry to ground geometry. This procedure is performed by interpolating the backscattered power from slant range-cross range geometry to the ground-elevation geometry and requires the understanding of platform positions and terrain topography. Once the tomographic cube is converted to ground geometry, the multi-layered backscattered power stack is compensated for different normalization approaches. The algorithm for retrieving forest canopy height using the tomographic approach, developed and validated using airborne data collected over boreal and tropical forests [17,28,41], was used in this work. The key idea behind this approach is to investigate the shape formed by the distribution of backscatter power along the vertical direction, $(P(z, x, r))$, for each azimuth-range index. Here, we assume that the shape of the backscattered power distribution function along the vertical direction (at each azimuth-range index) can be broken down into three zones. The first zone represents the contribution of backscattering from the canopy layer, primarily from the phase center. As we move in the vertical direction from the phase center, the backscatter profile exhibits loss of power value resulting from diminishing forest canopy density. This constitutes the second zone, known as the power loss zone. The third zone lies above the power loss zone and does not have any association with the physical parameters. This is primarily due to the contribution of noise resulting in the backscattered power in this region. Now, to retrieve the tree height, we begin with the estimation of the phase center (H_c), an effective scattering center over which most of the backscattering power is concentrated, and it is given by:

$$H_c(x,r) = \arg\max_z \{P(z,x,r)\} \tag{13}$$

Then we estimate the power loss (K) from the phase center location along the upper envelope in the vertical direction to estimate the forest height (H). However, the value of power loss is unknown and has to be estimated. In this work, we have used CHM derived from LiDAR data for estimating the optimum value of power loss. This estimation procedure can be formulated as:

$$H(x,r) = \arg\min \{|P(z',x,r) - P(H_c,x,r) - K|\} \tag{14}$$

Here, $P(H_c, x, r)$ is backscattered power at H_c and $P(z', x, r)$ is backscattered power values for elevation ranging from H_c to the upper limit of the profile.

4. Results and Discussions

The multi-baseline data stack was acquired with short temporal baselines obtained within a total span of 2 h. Additionally, no rain events were recorded around the days of data acquisition and hence no or negligible temporal decorrelation can be assumed. The compact, hybrid, and dual circular polarizations (DCP) stack was synthesized from the full polarimetric data and was used for further analysis. The holdout cross-validation approach was performed iteratively by selecting 75% as training and 25% as testing data, and accuracy was assessed using root-mean-square error (RMSE) and Pearson coefficient (r_p). Numerous research has discussed the tomographic analysis of forest over the Paracou site in linear polarization mode [17,36,37,40,41]. However, for this study, from the point of view of tomographic analysis, we are more focused on the compact (PiH & PiV), hybrid (RH & RL), and DCP (RR & RL) modes. The analysis of tomograms is restricted to the patch of the SAR image shown in Figure 2 because all the validation plots and LiDAR data available falls within this region. We investigated the forest vertical profiles using tomograms estimated over the kernel size of 9 × 9 pixels in range-azimuth direction, corresponding to an area 9.0 m × 11.205 m (~100 m^2). The vertical resolution of the BP approach depends on the look angle variations from the near-range to the far-range, resulting in variations of Rayleigh resolution from approximately 20 m within the image. However, over the ROI shown in Figure 2, the vertical resolution varies from approximately 20 m in near-range (4255 m) to 30 m in far-range (6255 m) of ROI. However, for the Capon and MUSIC

estimators, we performed the retrieval of backscatter by sampling at 1 m in the vertical direction. The tomograms are normalized such that summation of backscattered power along the elevation direction is one for each voxel, assisting a better visual interpretation of profiles. The LiDAR-derived canopy heights are overlaid over the tomographic profiles for the validation of profile estimation.

4.1. Tomographic Profile and the Multi-Layer Stack

Figure 4 represents the tomographic profiles using BP (Figure 4a,b), Capon (Figure 4c,d), and MUSIC (Figure 4e,f) estimation approaches along the range direction (of a constant azimuth transect aa' x = 1839 m) at PiH and PiV polarizations. The general observation is that the signal was able to penetrate the volumetric layer to the ground and the scattering is observed from both vegetation and ground surface for all polarizations, but the total backscattered power varies with transmit-receive configuration. It was observed that V-receive (HV, PiV, RV) and cross-polar channels (HV, RL) displayed strong volume contribution with significant contribution from the ground. Further, H-receive (HH, PiH, RH) and co-polar channels (HH, VV, RR) show dominant ground scattering behavior, with HH exhibiting the strongest of them all. The tomographic profiles, estimated using Capon in the range direction for a mid-azimuth section cut (aa' x = 1839 m), displays a similar overall vertical profile as the BP approach. They are able to better resolve the scatterers and suppress sidelobes; however, they exhibit a loss of radiometric accuracy. For tomographic profiles estimated using MUSIC, we have used a second-order estimator, which allows us to retrieve both the ground and canopy scattering components. The second-order estimator is constructed by spanning the noise subspace obtained by selecting the Eigenvectors corresponding to N-2 smallest Eigenvalues. This allows the MUSIC estimator to locate the position of the scatterer's phase centers, resulting in better discretization of targets. Figure 4 shows that the ground and canopy top positions can be clearly demarcated with suppressed sidelobes for the MUSIC estimator, indicating that it may assist better retrieval of terrain and height information.
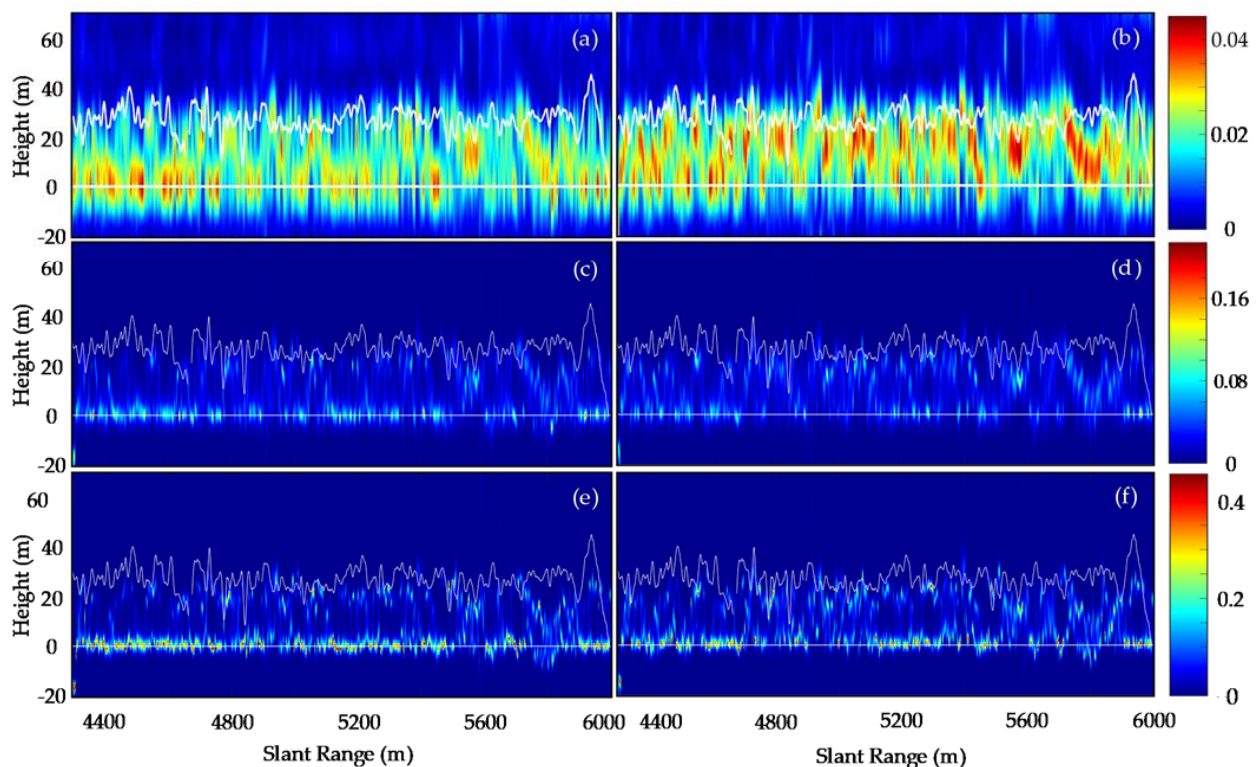

Figure 4. A tomographic profile over Paracou forest at PiH and PiV (left to right) polarimetric channel for back-projection (BP) (**a**,**b**), Capon (**c**,**d**) and MUSIC (**e**,**f**) estimators. The panels have been normalized so that the sum along the elevation direction is unitary, and white lines represent LiDAR Height values.

Each tomographic layer in the stack is related to backscattered power at a different height (0 m, 10 m, 20 m, 30 m and so on), which are ground steered to the corresponding terrain height values. The analysis of the multi-layer tomographic cube exhibited the influence of terrain slope on the backscattering power at different layers. For the BP approach, it is observed that the top and bottom layers of the stack displayed a strong correlation with terrain slope, while the intermediate layers showed less sensitivity to terrain slope. However, the backscattered power at different layers of tomographic cubes using Capon or MUSIC showed no or negligible correlation with terrain slope, as shown in Figure 5. This is because the super-resolution estimators provide pseudo-spectrums such that the radiometric characteristics of the image are no longer preserved and therefore result in a lack of sensitivity to the effect of the terrain slope. Similarly, for the middle layers, the BP estimators show increased sensitivity to different scattering components of the forest, whereas, in contrast, Capon and MUSIC show less sensitivity. Hence, to achieve a meaningful relationship between backscatter values and the forest vertical structure and tree height, radiometric compensation (R.C.) was applied to the tomographic cubes for the super-resolution techniques. From Figure 5, it can be observed that the implementation of R.C. results in a significant correlation between the backscattered power and terrain slope. This is primarily due to the influence of ground contribution resulting from the scatterer's orientation within the pixel of the master image used for compensating the tomographic layers. This effect was much more prominent in the ground and top layers than in the middle layers. Additionally, it was observed that the radiometric compensation in the co-polar channels is more influenced by the ground contribution than it is in the cross-polar channels.

Figure 6 displays the vertical profiles of the tomograms generated for different polarizations over the 1-ha resolution validation plots using different estimators. The profiles of Capon and MUSIC displays the radiometrically calibrated backscattered power of the tomogram. Figure 6 shows that MUSIC and Capon estimators provide better separation between the ground and volumetric contribution compared to the BP approach. It can be observed that the maximum mean backscattered power for the volume contribution lies between 20–21 m for all the polarization channels for different estimators. Additionally, it is observed that the BP estimated backscattered power showed a dynamic range (P_{min}, P_{max}) of -20 to -7 dB, whereas Capon and MUSIC displayed a larger dynamic range of -32 to 3 dB and -11 to 26 dB, respectively, depending on the polarization. Figure 6 also shows that the ground layer displays a strong backscatter. This is primarily due to the fact that the ground scattering and the phase center of ground-trunk interactions is located on the ground over flat terrain [36,37].
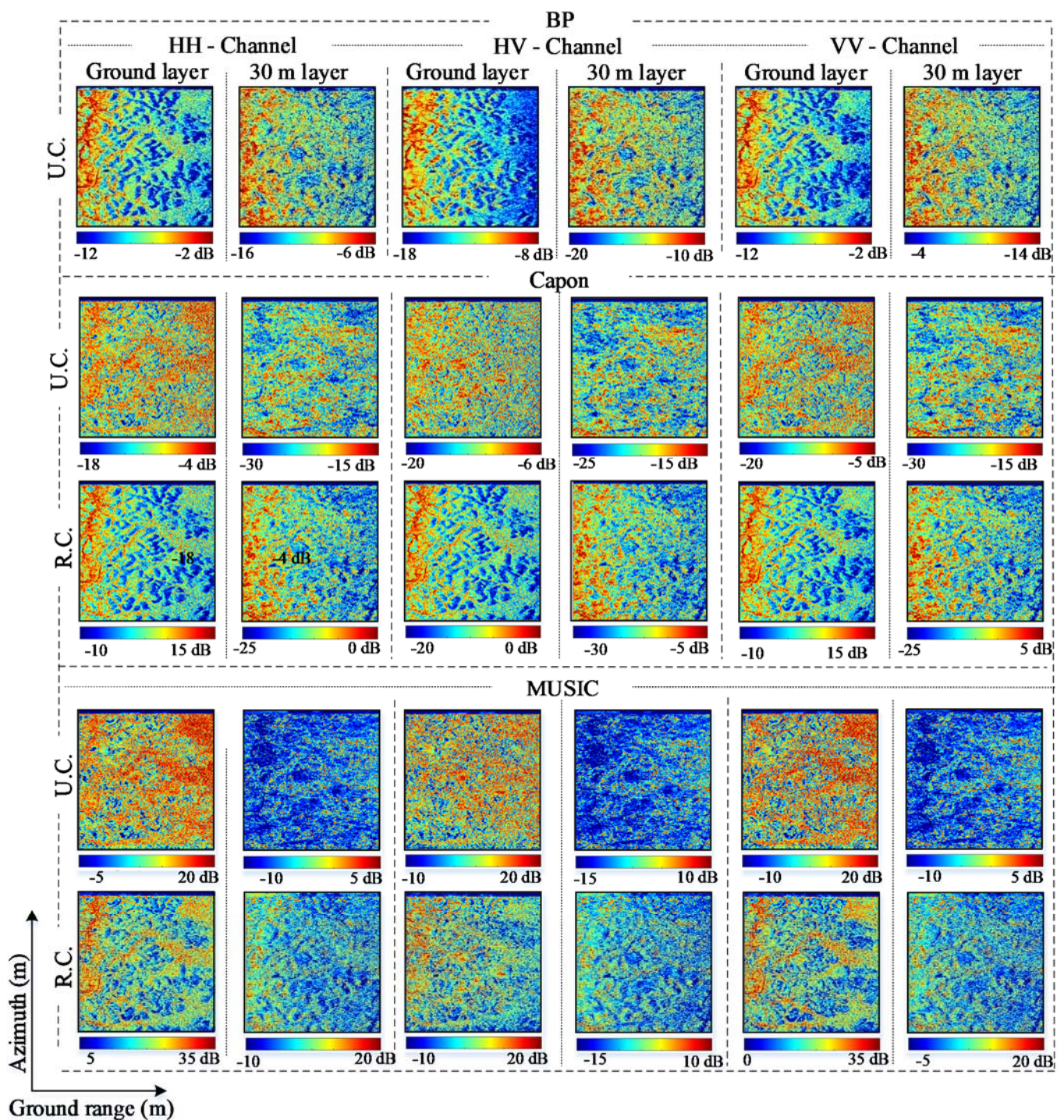
Figure 5. Tomographic layers over the Paracou ROI-HH, HV, VV backscattered power associated with ground and 30 m layers estimated using BP, Capon and MUSIC estimator. Here, U.C., R.C. represent the uncorrected and radiometric compensated backscattered power of different tomographic layers.

To assess the impact of slope and volumetric normalization on the backscattered power of different layers, we consider the uncompensated backscattered power of BP, and radiometrically calibrated Capon and MUSIC backscattered power (mentioned as uncompensated in Figure 6 to maintain consistency in naming convention). Figure 7 displays the backscattered power at 0 and 30 m layers for PiV polarization. It is observed that, for the BP approach, the ground layer shows a strong correlation with the terrain slope when compared to Capon and MUSIC. Similar behavior is observed in the top layers but to a

lesser extent. The intermediate layers are less affected by slope for all estimators. However, normalizing the intermediate layers with respect to slope and volume resulted in decreased backscatter values for BP and not much variation for Capon and MUSIC estimators.
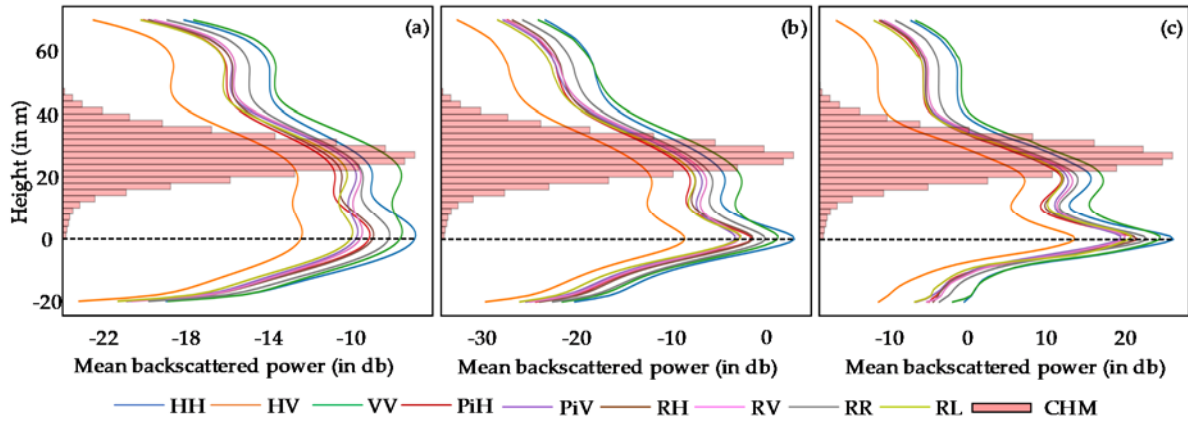

Figure 6. Power spectra of (**a**) BP and radiometrically calibrated (**b**) Capon and (**c**) MUSIC estimators over the field plots of the Paracou site. The spectra at HH, HV, VV, PiH, PiV, RH, RV, RR and RL polarization channels are derived at 1 ha. resolution, and the histogram of canopy heights derived from the LiDAR data is represented in red.
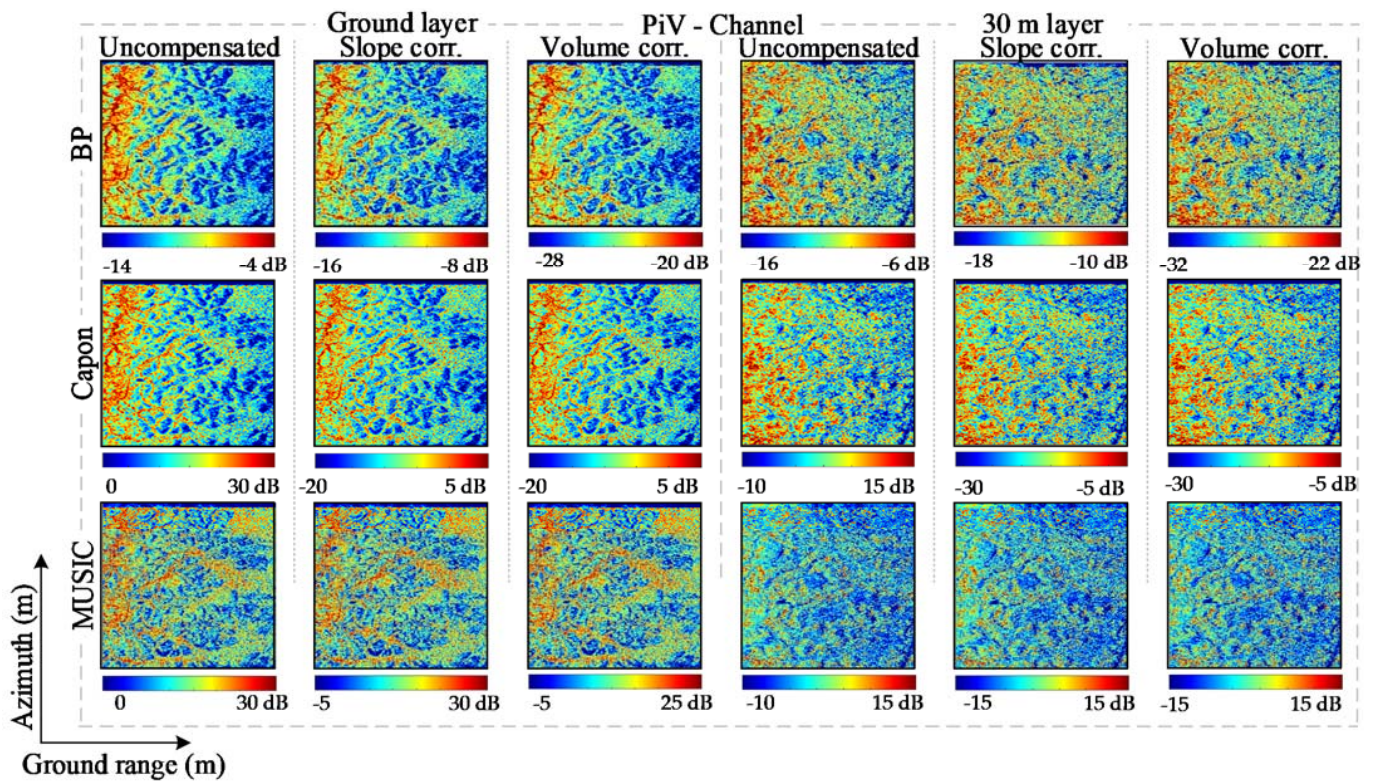

Figure 7. Tomographic layers over the Paracou ROI-PiV backscattered power associated with ground and 30 m layers estimated using BP, Capon and MUSIC estimators. Here, Uncompensated, Slope corr. and Volume corr. represents the uncorrected, slope, and volume compensated backscattered power for ground and 30 m tomographic layers.

4.2. Tomographic Tree Height Estimation

The tree height is estimated with the assistance of LiDAR-derived CHM values over the study site. The power loss value, in Equation (12), is varied from 0 to −15 dB for BP and Capon and 0 to −30 dB for MUSIC estimator. Then the error statistics are calculated with

respect to LiDAR-derived CHM over the training site. The power loss that corresponds to the minimum root mean squared error (RMSE) value is selected as the optimum power loss value. Finally, tree height for the rest of the image is estimated using the optimum K value and validated over the testing sites. In order to understand the impact of different compensation techniques on retrieval of tree height, we begin with comparing the results of the Capon and MUSIC estimator with and without radiometric corrections. Applying the radiometric correction resulted in increased power loss value for MUSIC; however, for Capon, the minimal trend is shown. The height estimation from radiometrically corrected backscattered power resulted in increased RMSE values, especially prominent in the co-polarization channels at 1-ha resolution. Additionally, there was no difference in RMSE of tree height values estimated using the uncompensated and slope compensated backscattered power of the BP approach. However, the height estimates from volume backscattered power displayed significantly higher RMSE values compared to its counterpart, as seen in Figure 8d–f.
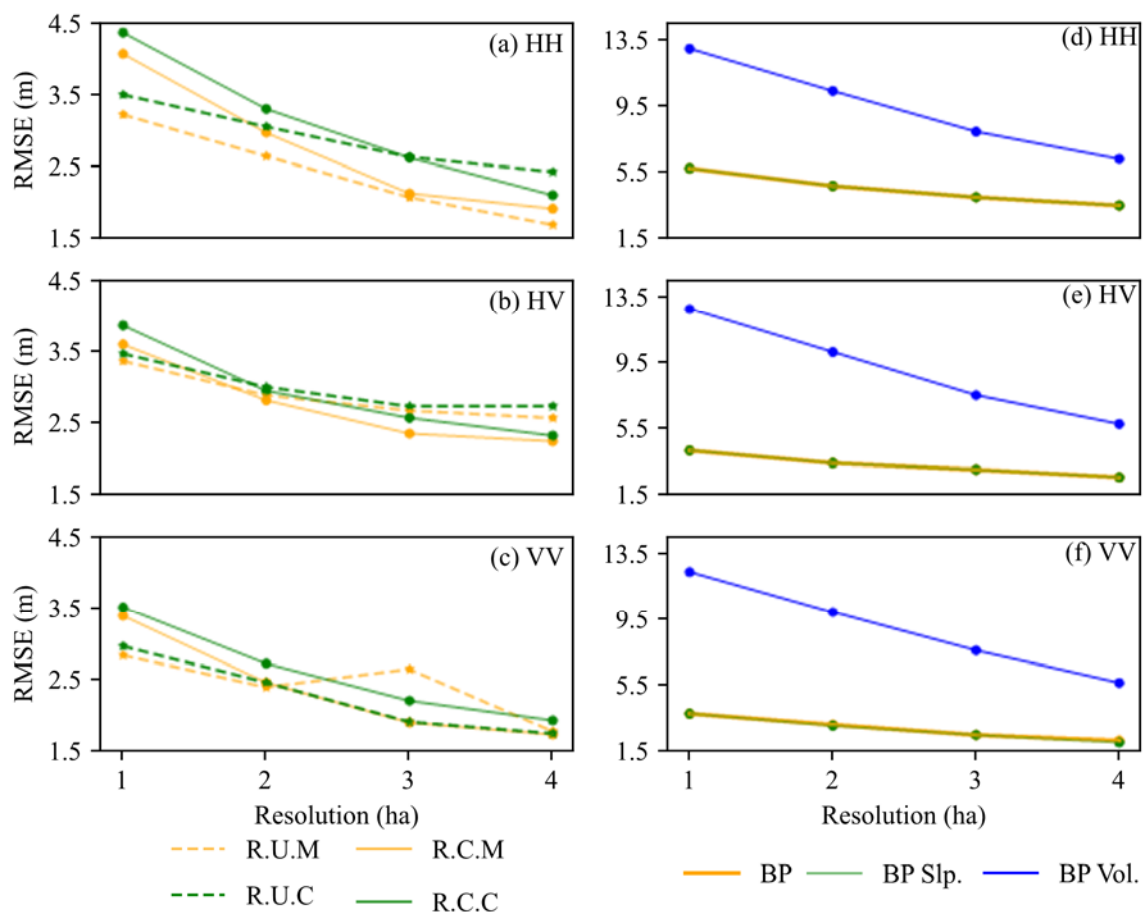

Figure 8. Comparison of RMSE of tree height estimation using backscattered power using different tomographic compensation approaches. (**a–c**) radiometrically uncorrected Capon (R.U.C. in dashed Green), radiometrically corrected Capon (R.C.C. in solid green), radiometrically uncorrected MUSIC (R.U.M in dotted orange), and radiometrically corrected MUSIC (R.C.M in solid orange). (**d–f**) uncorrected (orange), slope (green) and volume (blue) corrected backscattered power using the Back-projection approach.

Here, we make use of the tree height estimated using uncompensated backscattered power for comparison of error statistics between estimators. Figure 8 displays the *RMSE* and R^2 of tree heights estimated using tomographic backscattered power at PiH and PiV polarizations. For each polarization, the minimum RMSE value was achieved for a power loss value with respect to a phase center height that falls within -2.88 ± 0.50, -10.17 ± 0.83 and -17.64 ± 0.79 dB for BP, Capon and MUSIC estimator, respectively.

Figure 9 shows that the increase in resolution not only improved RMSE value but also the reliability of estimates. It was possible to retrieve the canopy height with an overall accuracy of RMSE of about 12% at 1-ha resolution to 6.5% at 4-ha of average LiDAR measured mean top canopy height, as shown in Table 1. Tree height retrieval using the MUSIC slightly outperforms Capon for all polarization channels, with BP performing the worst of the three. The right circular transmits consistently performed better, along with the VV polarization. The validation of tree height estimates using different estimators was also performed for different slope bins. It was noted that the bias of tree height estimates shows a clear correlation with terrain slope. In the BP approach, most of the terrain areas displaying positive slopes underestimated the tomographic-based heights compared to the LiDAR canopy heights. Conversely, for most of the cases with negative slopes, the tomographic-based height estimates showed higher values compared to LiDAR canopy heights, resulting in an overestimation of forest heights. However, Capon and MUSIC both show smaller bias values, with less dispersion.
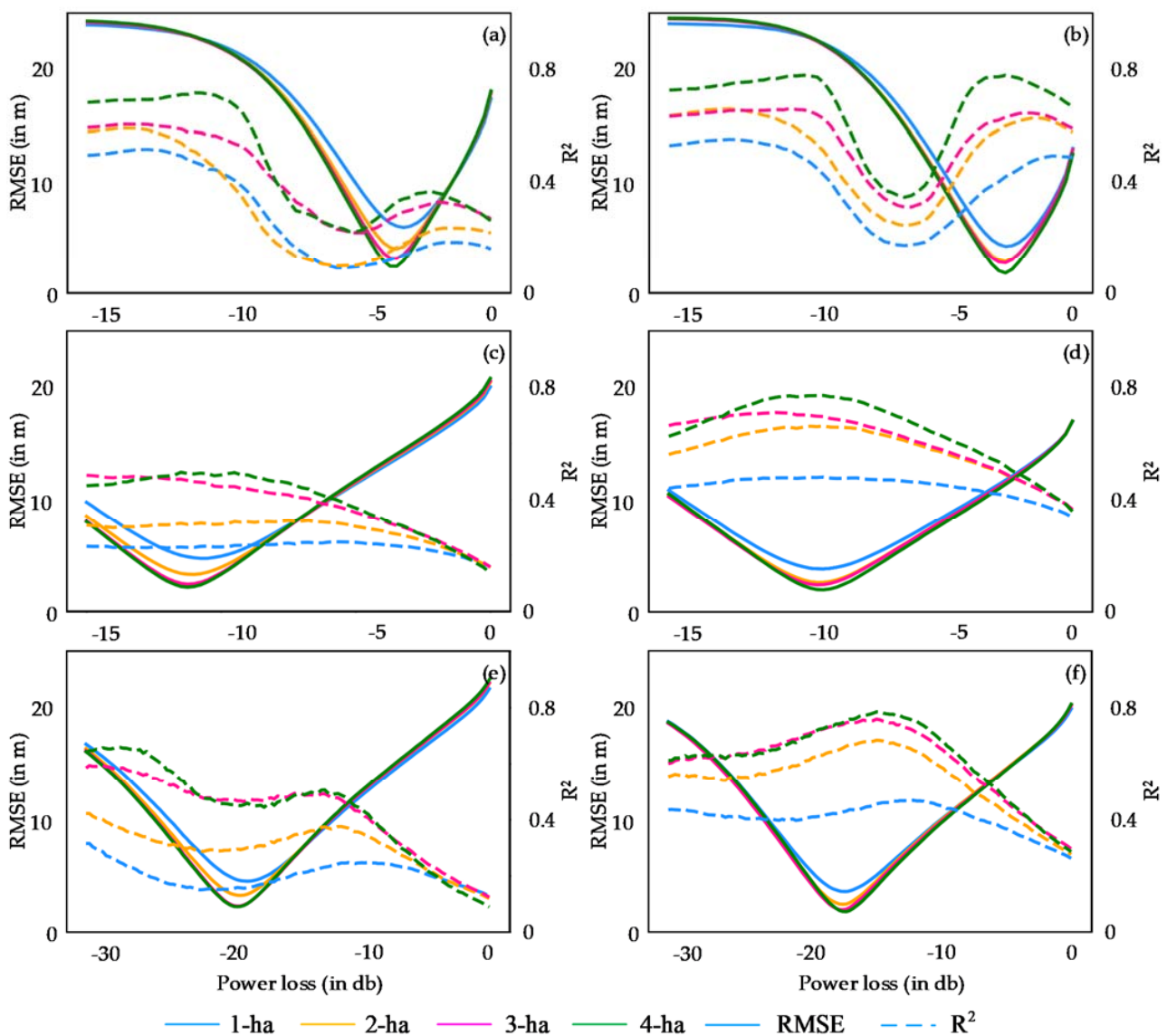

Figure 9. RMSE (solid line) and R^2 (dashed line) of tomographic tree heights estimated at 1-ha (blue), 2-ha (orange), 3-ha (pink), and 4-ha (green) resolution PiH and PiV polarizations using BP (**a**,**b**), Capon (**c**,**d**) and MUSIC (**e**,**f**) estimators, respectively for different power loss values with respect to phase center height. The power loss (PL) values vary from −15 to 0 dB for BP and Capon and −30 to 0 dB for MUSIC.

Table 1. Validation of forest tree height estimates at 4-ha resolution for different polarizations. Color coding by *RMSE* value relative to mean LiDAR tree height over the plots: white for RMSE ≤ 10%, gray for 10% < RMSE < 15% and dark gray for RMSE ≥ 15% of mean LiDAR tree height.

Polarization	BP RMSE (Power loss, r_p)	Capon RMSE (Power loss, r_p)	MUSIC RMSE (Power loss, r_p)
HH	3.54 (−3.75, 0.983)	2.11 (−11.5, 0.994)	1.92 (−18.75, 0.995)
HV	2.59 (−2.5, 0.991)	2.33 (−9.25, 0.992)	2.25 (−16.5, 0.993)
VV	2.19 (−2.25, 0.993)	1.94 (−9.5, 0.994)	1.74 (−17.0, 0.995)
PiH	3.51 (−3.5, 0.983)	2.54 (−11.0, 0.991)	2.31 (−18.5, 0.992)
PiV	2.27 (−2.5, 0.993)	2.06 (−9.25, 0.994)	1.71 (−16.75, 0.996)
RH	2.86 (−3.25, 0.989)	1.92 (−10.75, 0.995)	1.77 (−18.25, 0.995)
RV	2.11 (−2.5, 0.994)	2.13 (−9.75, 0.994)	1.86 (−17.25, 0.995)
RR	3.02 (−3.5, 0.987)	1.89 (−11.0, 0.995)	1.79 (−18.75, 0.995)
RL	2.3 (−2.25, 0.993)	1.91 (−925, 0.995)	1.77 (−17.0, 0.995)

4.3. Forest Vertical Profile and Tomographic Metric

The forest vertical profiles in Figures 10 and 11 are from Plots 7, 8, 13 and 16 in Figure 2. From Figure 10q–t, it is observed that Plots 7 and 8 characterize low biomass density, whereas Plots 13 and 16 display higher biomass density. These plots are used to understand the impact of different compensation approaches on the vertical profiles of different estimators with different forest densities. Further, the histogram of tree heights derived from LiDAR CHM over the plots are shown to compare the distribution of tree structure within the plots. The maxima of the histogram of LiDAR CHM was observed around 22, 26, 32 and 34 m for Plots 7, 8, 13 and 16, respectively. Figure 10 shows the forest vertical profiles for HH (blue), HV (orange) and VV (green) polarization channels from uncompensated and radiometrically compensated backscatter power using Capon and MUSIC estimators. It is observed that, for uncompensated Capon and MUSIC, backscattered power at different polarization shows a similar response. The distinct local maxima are found at ground level of the vertical profile for all plot, indicating the capability of the P-band to penetrate to ground level. For low-density plots, the demarcation of canopy level was found to be difficult, especially when using the Capon estimator. This weaker response to the canopy layer can be attributed to the sparse vegetation component in the upper compartment of vegetation over these plots. However, for Plots 13 and 16, the canopy maxima were observed around 24 and 22 m for both the Capon and the MUSIC estimator, respectively. The radiometric correction resulted in an increase in backscatter value of profiles with a shift in maxima of canopy layer between 27–29 and 24–26 for Plots 13 and 16 for both the Capon and the MUSIC estimators. Additionally, the cross-polarized channel shows lower values of intensity along with the vertical profile compared to the co-polarized channels for both estimators after radiometric compensation.

Figure 11 shows the forest vertical profiles for PiH polarization with no (red), slope (green) and volume (cyan) compensated backscatter power using BP, radiometrically corrected Capon, and MUSIC estimators. It is observed that, for Plots 13 and 16, irrespective of the approach used, the maxima is achieved around a similar height, with Capon and MUSIC distinctly demarcating the local maxima and canopy layer. Compensating for slope and volume resulted in a decrease in the backscatter values of profiles with similar profiles pattern. The higher decrease in volume compensated BP profile could be related to coarse resolution in the vertical direction. For the radiometrically compensated Capon and MUSIC estimators, the effect of slope and volume compensation resulted in much lesser variation compared to BP, which can be related to the finer spacing in the vertical direction for the super-resolution techniques.
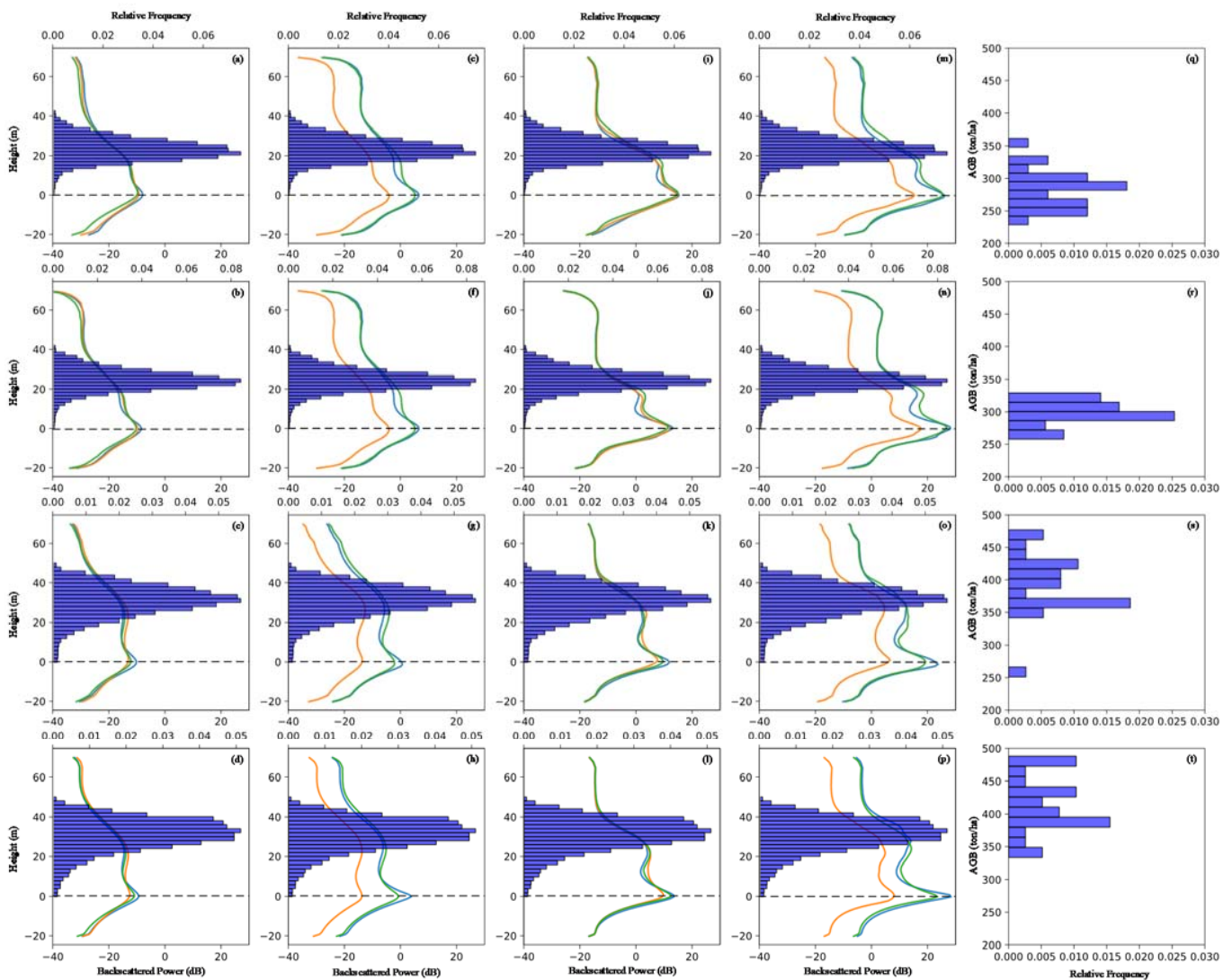
Figure 10. Forest vertical profiles from P-band tomographic data of low density (Plots 7 and 8) and high density (Plots 13 and 16) AGB plots for HH (blue), HV (orange), and VV (green) polarization channels from uncompensated and radiometrically compensated backscatter power using Capon and MUSIC estimators at 2-ha resolution. The tree height histogram (navy blue) from LiDAR CHM is also provided to give a representative tree height within the plot: (**a–d**) uncompensated Capon profiles of Plots 7, 8, 13, and 16; (**e–h**) radiometrically compensated Capon profiles of Plots 7, 8, 13 and 16; (**i–l**) uncompensated MUSIC profiles of Plots 7, 8, 13 and 16; (**m–p**) radiometrically compensated MUSIC profiles of Plots 7, 8, 13 and 16; (**q–t**) LiDAR derived AGB of Plots 7, 8, 13 and 16.
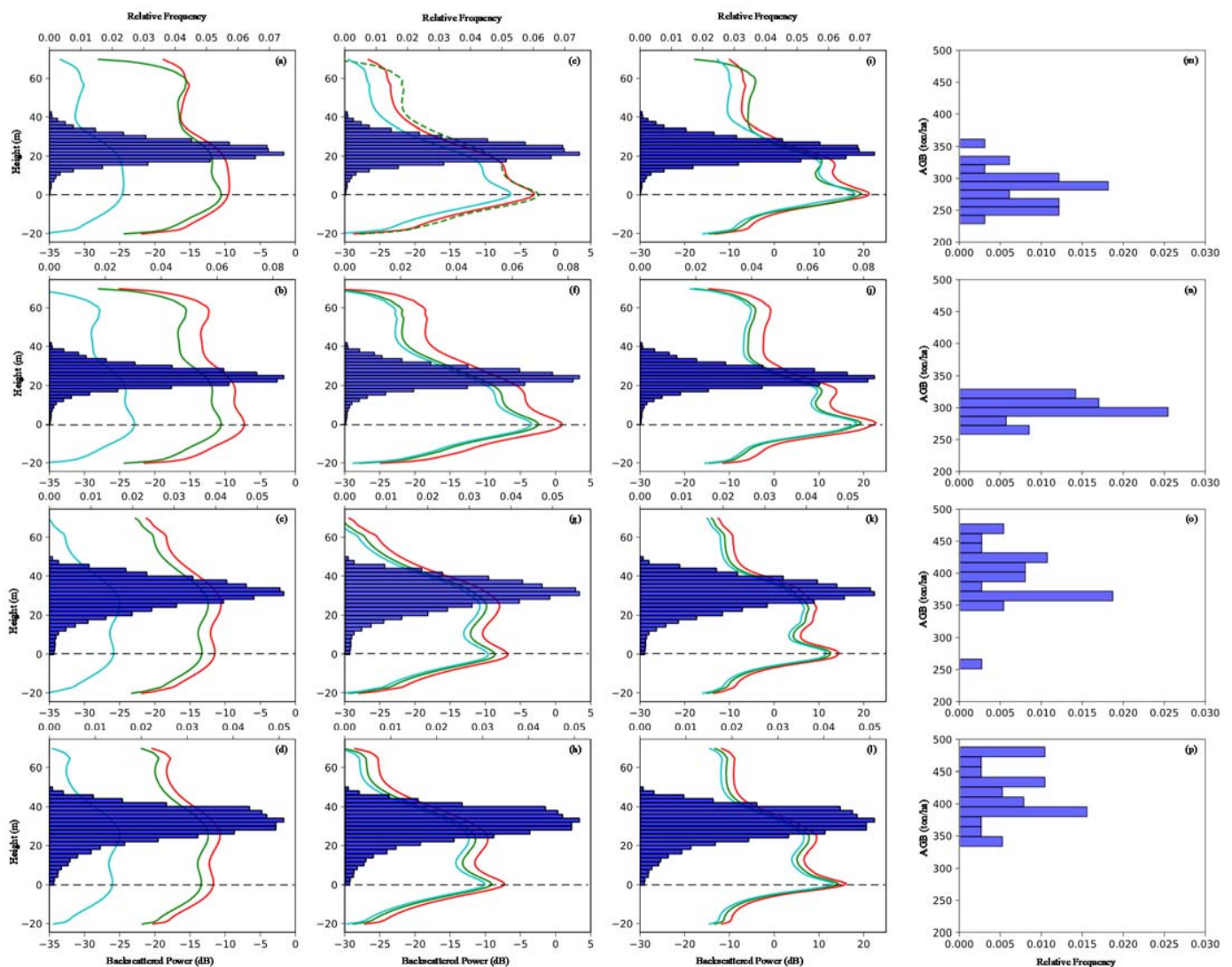
Figure 11. Forest vertical profiles from P-band tomographic data of low density (Plots 7 and 8) and high density (Plots 13 and 16) AGB forest plots for PiV polarization channels with uncompensated (red), slope (green) compensated, and volume (cyan) compensated backscattered power derived using BP, Capon, and MUSIC estimators at 2-ha resolution. The tree height histogram (navy blue) from LiDAR CHM is also provided to give a representative tree height within the plot: (**a–d**) BP uncompensated, slope, and volume compensated profiles of Plots 7, 8, 13 and 16; (**e–h**) Capon uncompensated, slope, and volume compensated of Plots 7, 8, 13 and 16; (**i–l**) MUSIC uncompensated, slope, and volume compensated profiles of Plots 7, 8, 13 and 16; (**m–p**) LiDAR derived AGB of Plots 7, 8, 13 and 16.

As we know that the tomographic layer provides the 3D distribution of backscattered power of a volumetric media, we derive a tomographic metric, integrated tomographic power ($P_{I_{pq}}$) by integrating the backscattered power along the z-direction from half of the vertical resolution from the ground to the tree height. The lower cut-off of half of the vertical resolution was selected in order to reduce the impact of ground and double-bounce contribution, which perturb the backscattered power at the lower tomographic level. Figure 12a represents the uncompensated and radiometrically compensated integrated power using the Capon and MUSIC estimators. Figure 12b shows tomographic integrated power using BP, radiometrically corrected Capon and MUSIC estimators with uncompensated, slope and volume compensation. It is noted that there is a decrease in backscatter power from near- to far-range for all the estimators after slope and volume compensation. The large decrease in integrated backscatter value after volumetric compensation over BP can be attributed to the vertical resolution of the BP estimator.
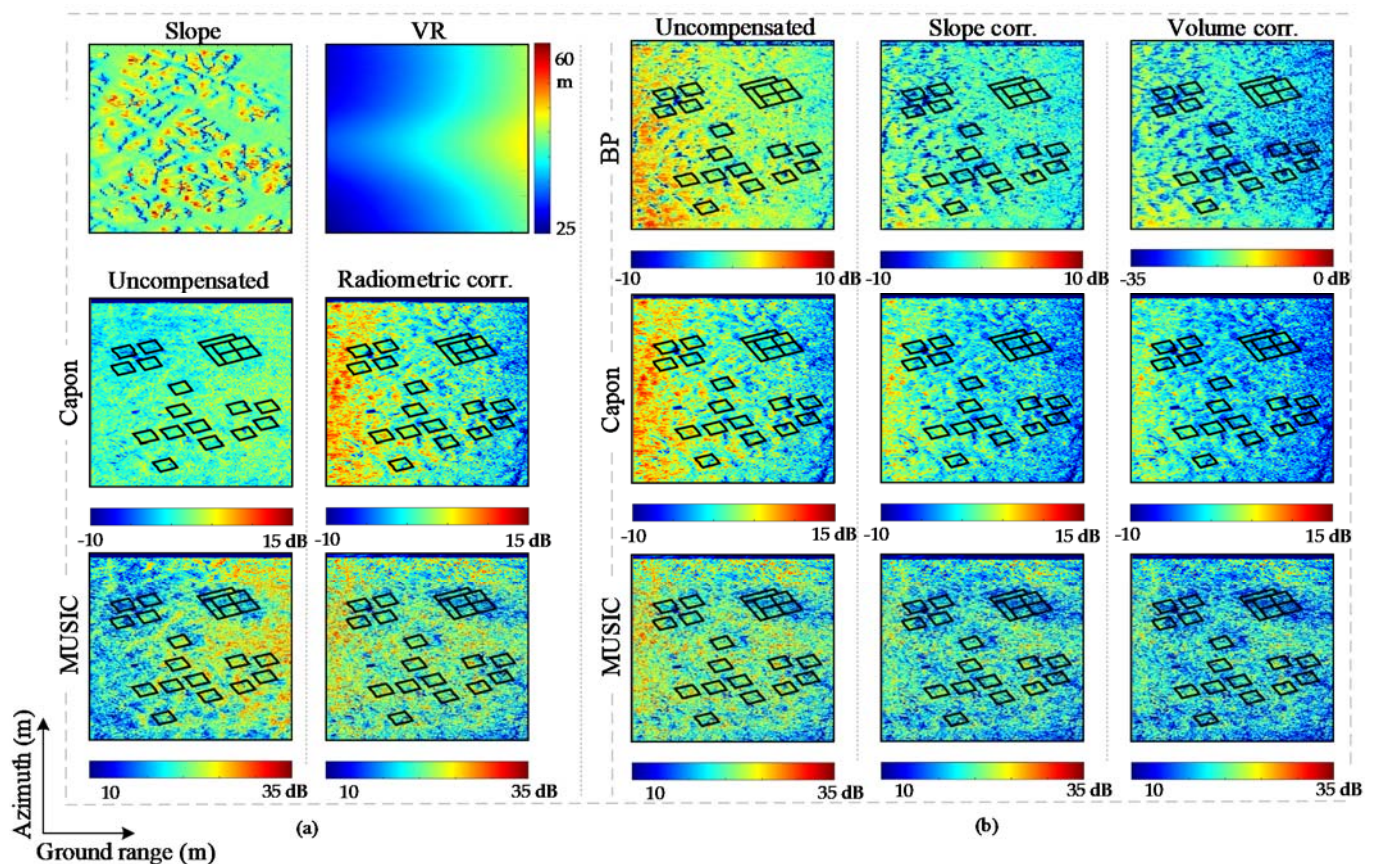
Figure 12. Tomographic derived metric over the Paracou ROI-HV backscattered power derived by integrated along the z-direction between half of the vertical resolution from the ground to tree height: (**a**) uncompensated and radiometrically compensated integrated power using Capon and MUSIC. The top left image represents the slope and the top right represents the vertical resolution. (**b**) uncompensated (represents radiometrically corrected for Capon and MUSIC). Uncompensated, Slope corr., and Volume corr. represent the uncorrected, slope, and volume compensated integrated power using BP, Capon, and MUSIC estimator.

5. Conclusions

In this study, we present the comparison of different P-band tomographic SAR processing and radiometric compensation techniques on the retrieval of the forest canopy height and vertical profile over a tropical forest site in French Guiana, with high biomass density variations. The tomographic P-band BP, Capon and MUSIC profiles at different polarizations showed a good correlation with the LiDAR CHM. The horizontal receive and co-polar channels better display the contribution of ground scattering, whereas the volume contribution is highlighted in V receive and cross-polar channels. The impact of different backscatter compensation approaches on parameter estimation was discussed and validated at different spatial scales relevant to the BIOMASS mission observational configuration. The performance of forest height retrieval using P-band SAR data, assisted by LiDAR CHM at different tomographic estimator- and polarization-resolutions was compared and validated. The RMSE values of 1.71 m and 1.74 m were achieved using PiV and VV polarization using the MUSIC estimator at 4-ha resolution, with corresponding R^2 values of 0.996 and 0.995, respectively. It is observed that estimating forest height from radiometric or slope and volume compensated backscattered power does not significantly improve the estimates, but rather resulted in the degradation of estimates in most cases. Additionally, the height estimates from different polarizations fall within the error range, suggesting that the scattering mechanisms seem to have a minor effect on polarization. However, this needs to be further investigated. The analysis of forest vertical profile displayed strong contribution from the ground level. The plots with higher biomass density

displayed stronger canopy demarcation compared to sparse density plots. Compared to BP, Capon and MUSIC profiles showed a strong performance in demarcating the scattering contributions. Applying radiometric correction to Capon and MUSIC profiles resulted in the increase in backscatter intensity along the vertical profile, with the co-polar channel showing higher increase values. Conversely, the slope and volume compensation resulted in the decrease in backscatter power of the profile, with volumetric compensation of BP showing a larger decline, which could be related to coarse vertical resolution. Similar behavior was observed for the tomographic-derived metric. Note that, in this study, the SAR data are used in their original bandwidths; any bandwidth reduction for space observations (e.g., 6 MHz for the BIOMASS mission) will impact the corresponding R^2 and *RMSE* but will not change the overall relative performance of the TomoSAR techniques demonstrated here.

Author Contributions: Conceptualization, N.R., S.S. and S.T.; Formal analysis, N.R., S.S., S.T., M.M.d. and O.D.; Investigation, N.R., S.S. and M.M.d.; Methodology, N.R. and S.T.; Resources, S.S., S.T. and M.M.d.; Software, N.R. and S.T.; Supervision, S.S., S.T. and O.D.; Validation, N.R. and S.S.; Visualization, N.R. and S.S.; Writing—original draft, N.R.; Writing—review & editing, S.S., S.T. and O.D. All authors have read and agreed to the published version of the manuscript.

Conflicts of Interest: The authors declare no conflict of interest.

References

1. Mitchard, E.T.A. The tropical forest carbon cycle and climate change. *Nature* **2018**, *559*, 527–534. [CrossRef]
2. Cramer, W.; Bondeau, A.; Schaphoff, S.; Lucht, W.; Smith, B.; Sitch, S. Tropical forests and the global carbon cycle: Impacts of atmospheric carbon dioxide, climate change and rate of deforestation. *Philos. Trans. R. Soc. Lond. Ser. B Biol. Sci.* **2004**, *359*, 331–343. [CrossRef] [PubMed]
3. Liang, S.; Wang, J. *Advanced Remote Sensing: Terrestrial Information Extraction and Applications*, 2nd ed.; Liang, S.N., Wang, J., Eds.; Academic Press: London, UK, 2020; ISBN 9780128158265.
4. Spies, T.A. Forest Structure: A Key to the Ecosystem. *Northwest Sci.* **1998**, *72*, 34–36.
5. Bongers, F. Methods to assess tropical rain forest canopy structure: An overview. *Plant Ecol.* **2001**, *153*, 263–277. [CrossRef]
6. Giri, C.; Pengra, B.; Zhu, Z.; Singh, A.; Tieszen, L.L. Monitoring mangrove forest dynamics of the Sundarbans in Bangladesh and India using multi-temporal satellite data from 1973 to 2000. *Estuar. Coast. Shelf Sci.* **2007**, *73*, 91–100. [CrossRef]
7. Nicotra, A.B.; Chazdon, R.L.; Iriarte, S.V.B. Spatial Heterogeneity of Light and Woody Seedling Regeneration in Tropical Wet Forests. *Ecology* **1999**, *80*, 1908–1926. [CrossRef]
8. Purves, D.; Pacala, S. Predictive models of forest dynamics. *Science* **2008**, *320*, 1452–1453. [CrossRef]
9. Thom, D.; Rammer, W.; Seidl, R. The impact of future forest dynamics on climate: Interactive effects of changing vegetation and disturbance regimes. *Ecol. Monogr.* **2017**, *87*, 665–684. [CrossRef] [PubMed]
10. Pan, Y.; Birdsey, R.A.; Fang, J.; Houghton, R.; Kauppi, P.E.; Kurz, W.A.; Phillips, O.L.; Shvidenko, A.; Lewis, S.L.; Canadell, J.G.; et al. A large and persistent carbon sink in the world's forests. *Science* **2011**, *333*, 988–993. [CrossRef] [PubMed]
11. Mitchard, E.T.; Saatchi, S.S.; Baccini, A.; Asner, G.P.; Goetz, S.J.; Harris, N.L.; Brown, S. Uncertainty in the spatial distribution of tropical forest biomass: A comparison of pan-tropical maps. *Carbon Balance Manag.* **2013**, *8*, 10. [CrossRef] [PubMed]
12. Aghababaei, H.; Ferraioli, G.; Ferro-Famil, L.; Huang, Y.; Mariotti d''Alessandro, M.; Pascazio, V.; Schirinzi, G.; Tebaldini, S. Forest SAR Tomography: Principles and Applications. *IEEE Geosci. Remote Sens. Mag.* **2020**, *8*, 30–45. [CrossRef]
13. Cazcarra-Bes, V.; Tello-Alonso, M.; Fischer, R.; Heym, M.; Papathanassiou, K. Monitoring of Forest Structure Dynamics by Means of L-Band SAR Tomography. *Remote Sens.* **2017**, *9*, 1229. [CrossRef]
14. Moussawi, I.; Ho Tong Minh, D.; Baghdadi, N.; Abdallah, C.; Jomaah, J.; Strauss, O.; Lavalle, M.; Ngo, Y.-N. Monitoring Tropical Forest Structure Using SAR Tomography at L- and P-Band. *Remote Sens.* **2019**, *11*, 1934. [CrossRef]
15. Reigber, A.; Moreira, A. First demonstration of airborne SAR tomography using multibaseline L-band data. *IEEE Trans. Geosci. Remote Sens.* **2000**, *38*, 2142–2152. [CrossRef]

16. Tebaldini, S. Single and Multipolarimetric SAR Tomography of Forested Areas: A Parametric Approach. *IEEE Trans. Geosci. Remote Sens.* **2010**, *48*, 2375–2387. [CrossRef]

17. Ho Tong Minh, D.; Le Toan, T.; Rocca, F.; Tebaldini, S.; Villard, L.; Réjou-Méchain, M.; Phillips, O.L.; Feldpausch, T.R.; Dubois-Fernandez, P.; Scipal, K.; et al. SAR tomography for the retrieval of forest biomass and height: Cross-validation at two tropical forest sites in French Guiana. *Remote Sens. Environ.* **2016**, *175*, 138–147. [CrossRef]

18. Cloude, S.R. Polarization coherence tomography. *Radio Sci.* **2006**, *41*. [CrossRef]

19. Treuhaft, R.N.; Madsen, S.N.; Moghaddam, M.; van Zyl, J.J. Vegetation characteristics and underlying topography from interferometric radar. *Radio Sci.* **1996**, *31*, 1449–1485. [CrossRef]

20. Treuhaft, R.N.; Siqueira, P.R. Vertical structure of vegetated land surfaces from interferometric and polarimetric radar. *Radio Sci.* **2000**, *35*, 141–177. [CrossRef]

21. Papathanassiou, K.P.; Cloude, S.R. Single-baseline polarimetric SAR interferometry. *IEEE Trans. Geosci. Remote Sens.* **2001**, *39*, 2352–2363. [CrossRef]

22. Pasquali, P.; Prati, C.; Rocca, F.; Seymour, M.; Fortuny, J.; Ohlmer, E.; Sieber, A.J. A 3-D SAR experiment with EMSL data. In *Quantitative Remote Sensing for Science and Applications, Proceedings of the 1995 International Geoscience and Remote Sensing Symposium, Congress Center, Firenze, Italy, 10–14 July 1995*; IGARSS 95, Quantitative Remote Sensing for Science and Applications; Institute of Electrical and Electronics Engineers, IEEE Service Center: New York, NY, USA; Piscataway, NJ, USA, 1995; ISBN 0780325672.

23. Huang, Y.; Ferro-Famil, L.; Reigber, A. Under-Foliage Object Imaging Using SAR Tomography and Polarimetric Spectral Estimators. *IEEE Trans. Geosci. Remote Sens.* **2012**, *50*, 2213–2225. [CrossRef]

24. Gini, F.; Lombardini, F.; Montanari, M. Layover solution in multibaseline SAR interferometry. *IEEE Trans. Aerosp. Electron. Syst.* **2002**, *38*, 1344–1356. [CrossRef]

25. Lombardini, F.; Reigber, A. Adaptive spectral estimation for multibaseline SAR tomography with airborne L-band data. In Proceedings of the IGARSS 2003 IEEE International Geoscience and Remote Sensing Symposium. (IEEE Cat. No.03CH37477), Toulouse, France, 21–25 July 2003; pp. 2014–2016, ISBN 0-7803-7929-2.

26. Fornaro, G.; Serafino, F.; Soldovieri, F. Three-dimensional focusing with multipass SAR data. *IEEE Trans. Geosci. Remote Sens.* **2003**, *41*, 507–517. [CrossRef]

27. Tebaldini, S. Forest SAR tomography: A covariance matching approach. In *Proceedings of the 2008 IEEE Radar Conference, Rome, Italy, 26–30 May 2008*; ISBN 9781424415380.

28. Tebaldini, S.; Rocca, F. Multibaseline Polarimetric SAR Tomography of a Boreal Forest at P- and L-Bands. *IEEE Trans. Geosci. Remote Sens.* **2012**, *50*, 232–246. [CrossRef]

29. Nannini, M.; Scheiber, R.; Moreira, A. Estimation of the Minimum Number of Tracks for SAR Tomography. *IEEE Trans. Geosci. Remote Sens.* **2009**, *47*, 531–543. [CrossRef]

30. Aguilera, E.; Nannini, M.; Reigber, A. A Data-Adaptive Compressed Sensing Approach to Polarimetric SAR Tomography of Forested Areas. *IEEE Geosci. Remote Sens. Lett.* **2013**, *10*, 543–547. [CrossRef]

31. Zhu, X.X.; Bamler, R. Demonstration of Super-Resolution for Tomographic SAR Imaging in Urban Environment. *IEEE Trans. Geosci. Remote Sens.* **2012**, *50*, 3150–3157. [CrossRef]

32. Aguilera, E.; Nannini, M.; Reigber, A. Wavelet-Based Compressed Sensing for SAR Tomography of Forested Areas. *IEEE Trans. Geosci. Remote Sens.* **2013**, *51*, 5283–5295. [CrossRef]

33. Aguilera, E.; Nannini, M.; Reigber, A. Multi-signal compressed sensing for polarimetric SAR tomography. In Proceedings of the 2011 IEEE International Geoscience and Remote Sensing Symposium, Sendai, Japan, 1–5 August 2011; pp. 1369–1372, ISBN 2153-7003.

34. Freeman, A.; Saatchi, S.S. On the detection of Faraday rotation in linearly polarized L-band SAR backscatter signatures. *IEEE Trans. Geosci. Remote Sens.* **2004**, *42*, 1607–1616. [CrossRef]

35. Rogers, N.C.; Quegan, S.; Kim, J.S.; Papathanassiou, K.P. Impacts of Ionospheric Scintillation on the BIOMASS P-Band Satellite SAR. *IEEE Trans. Geosci. Remote Sens.* **2014**, *52*, 1856–1868. [CrossRef]

36. Mariotti d'Alessandro, M.; Tebaldini, S. Phenomenology of P-Band Scattering from a Tropical Forest Through Three-Dimensional SAR Tomography. *IEEE Geosci. Remote Sens. Lett.* **2012**, *9*, 442–446. [CrossRef]

37. Mariotti d'Alessandro, M.; Tebaldini, S. Phenomenology of Ground Scattering in a Tropical Forest through Polarimetric Synthetic Aperture Radar Tomography. *IEEE Trans. Geosci. Remote Sens.* **2013**, *51*, 4430–4437. [CrossRef]

38. Bamler, R.; Philipp, H. Synthetic aperture radar interferometry. *Inverse Probl.* **1998**, *14*, R1–R54. [CrossRef]

39. Tebaldini, S.; Guarnieri, A.M. On the Role of Phase Stability in SAR Multibaseline Applications. *IEEE Trans. Geosci. Remote Sens.* **2010**, *48*, 2953–2966. [CrossRef]

40. Ho Tong Minh, D.; Le Toan, T.; Rocca, F.; Tebaldini, S.; D'Alessandro, M.M.; Villard, L. Relating P-Band Synthetic Aperture Radar Tomography to Tropical Forest Biomass. *IEEE Trans. Geosci. Remote Sens.* **2014**, *52*, 967–979. [CrossRef]

41. Ho Tong Minh, D.; Tebaldini, S.; Rocca, F.; Le Toan, T.; Villard, L.; Dubois-Fernandez, P.C. Capabilities of BIOMASS Tomography for Investigating Tropical Forests. *IEEE Trans. Geosci. Remote Sens.* **2015**, *53*, 965–975. [CrossRef]

42. Lombardini, F.; Cai, F.; Viviani, F.; Pasculli, D. Multidimensional SAR tomography for complex non-stationary scenes: COSMO-SkyMed urban and P-band forest results. In *Proceedings of the IEEE International Geoscience and Remote Sensing Symposium (IGARSS), Munich, Germany, 22–27 July 2012*; IEEE: Piscataway, NJ, USA, 2012; pp. 5206–5209, ISBN 978-1-4673-1159-5.

43. Nannini, M.; Scheiber, R. Height dependent motion compensation and coregistration for airborne SAR tomography. In *Proceedings of the 2007 IEEE International Geoscience and Remote Sensing Symposium, Barcelona, Spain, 23–27 July 2007*; IEEE: Piscataway, NJ, USA, 2007; pp. 5041–5044, ISBN 978-1-4244-1211-2.

44. Nannini, M.; Scheiber, R.; Horn, R.; Moreira, A. First 3-D Reconstructions of Targets Hidden Beneath Foliage by Means of Polarimetric SAR Tomography. *IEEE Geosci. Remote Sens. Lett.* **2012**, *9*, 60–64. [CrossRef]

45. Chen, Z.; Gokeda, G.; Yu, Y. *Introduction to Direction-Of-Arrival Estimation*; Artech House: Boston, MA, USA, 2010; ISBN 1596930896.

46. Stoica, P.; Moses, R.L. *Spectral Analysis of Signals*; Pearson/Prentice Hall: Upper Saddle River, NJ, USA, 2004; ISBN 0131139568.

47. Krim, H.; Viberg, M. Two decades of array signal processing research: The parametric approach. *IEEE Signal Process. Mag.* **1996**, *13*, 67–94. [CrossRef]

48. Saatchi, S.S.; van Zyl, J.J.; Asrar, G. Estimation of canopy water content in Konza Prairie grasslands using synthetic aperture radar measurements during FIFE. *J. Geophys. Res.* **1995**, *100*, 25481. [CrossRef]

49. van Zyl, J.J.; Chapman, B.D.; Dubois, P.; Shi, J. The effect of topography on SAR calibration. *IEEE Trans. Geosci. Remote Sens.* **1993**, *31*, 1036–1043. [CrossRef]

50. Molto, Q.; Rossi, V.; Blanc, L. Error propagation in biomass estimation in tropical forests. *Methods Ecol Evol* **2013**, *4*, 175–183. [CrossRef]

51. Chave, J.; Piponiot, C.; Maréchaux, I.; Foresta, H.D.; Larpin, D.; Fischer, F.J.; Derroire, G.; Vincent, G.; Hérault, B. Slow rate of secondary forest carbon accumulation in the Guianas compared with the rest of the Neotropics. *Ecol. Appl.* **2020**, *30*, e02004. [CrossRef]

52. Labriere, N.; Tao, S.; Chave, J.; Scipal, K.; Le Toan, T.; Abernethy, K.; Alonso, A.; Barbier, N.; Bissiengou, P.; Casal, T.; et al. In Situ Reference Datasets from the TropiSAR and AfriSAR Campaigns in Support of Upcoming Spaceborne Biomass Missions. *IEEE J. Sel. Top. Appl. Earth Obs. Remote Sens.* **2018**, *11*, 3617–3627. [CrossRef]

53. Reigber, A.; Prats, P.; Mallorqui, J.J. Refined Estimation of Time-Varying Baseline Errors in Airborne SAR Interferometry. *IEEE Geosci. Remote Sens. Lett.* **2006**, *3*, 145–149. [CrossRef]

54. Tebaldini, S.; Rocca, F. On the impact of propagation disturbances on SAR Tomography: Analysis and compensation. In Proceedings of the 2009 IEEE Radar Conference, Pasadena, CA, USA, 4–8 May 2009; 2009; pp. 1–6, ISBN 978-1-4244-2870-0.

55. Tebaldini, S.; Rocca, F.; Mariotti d'Alessandro, M.; Ferro-Famil, L. Phase Calibration of Airborne Tomographic SAR Data via Phase Center Double Localization. *IEEE Trans. Geosci. Remote Sens.* **2016**, *54*, 1775–1792. [CrossRef]

56. Mariotti d'Alessandro, M.; Tebaldini, S. Digital Terrain Model Retrieval in Tropical Forests through P-Band SAR Tomography. *IEEE Trans. Geosci. Remote Sens.* **2019**, *57*, 6774–6781. [CrossRef]